Effects of Aero-Propulsive Coupling on High Solidity Electric Ducted Fan Performance for Various Wing Integrations

Derek A. Safieh
Graduate Research Assistant
Georgia Institute of Technology
Atlanta, GA 30332, USA

Juergen Rauleder
Assistant Professor
Georgia Institute of Technology
Atlanta, GA 30332, USA

The increase in population in urban areas and their surroundings, combined with inefficient and saturated land routes, have sparked a booming interest in regional and urban air transportation options. Electric Ducted Fans (EDF) are expected to help these new concepts meet the ambitious goals set by the aviation industry. While most boundary layer ingestion propulsion methods, like EDFs, have been extensively studied at a system level, little attention has been given to decoupling EDF forces for various wing integrations. This study focuses on understanding the changes in performance that various aero-propulsive integrations have on the EDF, comparing leading edge and trailing edge EDF integrations to an isolated EDF. For both integration cases, the EDF power loading increased over the isolated case. This increase was greater for the higher advance ratios. The leading edge integration pitching moment showed a growing destabilizing moment similar to that of the isolated thruster for the upper surface integration, but showed a constant destabilizing behavior (independent of angle of attack) for the lower surface. While the pitching moment of the isolated case was destabilizing and increased in magnitude with increased angle of attack, the pitching moment of the trailing edge integrated EDF was mostly constant. For the upper surface this moment is stabilizing while for the lower surface its destabilizing. This shows the importance of understanding the EDF's aerodynamic characteristics as they might affect the overall lifting system characteristics. A high-frequency analysis using a short-time Fourier transform (STFT) on the system pitching moment and inlet acoustic signature showed similar dominant frequencies for the isolated EDF and leading edge integration for both the loads and acoustic data, but revealed the existence of new high and low frequency transient loads for the trailing edge integration. Both integration methods showed increases in performance and power reduction. The trailing edge integrated EDF required 12% less power (max value) than the isolated EDF, while the leading edge integrated EDF required 8% less power (max value) for the same operational conditions.

Nomenclature

A	Rotor disk area (m^2)
C_P	DC Power coefficient, $\frac{P}{\rho A(\Omega R)^3}$
C_T/C_P	Non-dimensional power loading
C_T	Thrust coefficient, $\frac{T}{\rho A(\Omega R)^2}$
M_Y	Pitching moment about rotor plane, M_Y (N-m)
P_{DC}	DC power (W)
R	Rotor radius (m)
T	EDF system Thrust (N)
Ω	Fan stage rotational speed (rad/s)
ρ	Air density (kg/m^3)

Presented at the 49th European Rotorcraft Forum, Bückeburg, Germany, September 5–7, 2023.

Introduction

Regional and urban transportation methods have seen a surge in usage due to the increase in population in urban areas and their surroundings. This has sparked a revolution in the way city planners design mobility platforms for current and new urban areas. With inefficient land routes already saturated, the next option is to travel by air. While the world has constructed a massive network of air routes over the years that connect continents in short periods of time, it is still landlocked for local commutes. For comparison, it takes 1.5 hours to travel from London to Munich by airplane but for the average Londoner, it takes 1.3 hours to get from home to work (Ref. 1). Cutting down travel time is one criterion for the push for air mobility, but the pollution and expensive operation costs produced by air routes have slowed their adoption. The European Environment Agency (EEA) reported that an airplane currently produces 6.7 times more CO_2 per passenger per kilometer traveled than a small car (Ref. 2). Due to this, the International Air Transport Association (IATA) approved the resolution to become Net-Zero emissions by 2050 during its 2021 General Meeting, quoting that 13% of this effort will be led by the introduction of new technologies in advanced aircraft configurations and propulsive systems (Ref. 3). It was also projected that by 2030, small aircraft for regional routes (200 km) will feature hybrid-electric or fully electric architectures (Ref. 3).

Wing integrated Electric Ducted Fans (EDF) have been on the rise as an enabling propulsive technology to help advanced concepts meet the ambitious goals set by the aviation industry. The lack of mechanical transmissions permits these propulsion devices to be integrated into different sections of the wings or fuselage, without the need for weighty shafts running through the structure. Furthermore, these new integration methods permit novel concepts to take advantage of aero-propulsive coupling effects that could help increase the efficiency of the overall vehicle. However, these aero-propulsive couplings may also yield performance penalties and jeopardize flight safety, and hence they need to be well understood.

The topic of boundary layer ingesting propulsion systems has been studied extensively with the goal to reduce fuel burn on subsonic and transonic flight. These studies were done on legacy and novel blended-wing body airframes alike. Uranga et al. (Ref. 4) showed a reduction in power required of 6% when using a Boundary Layer Ingestion (BLI) propulsion system mounted on the fuselage of similar size to an A320 jetliner. In that study, Uranga et al. positioned the thrusters in various locations at the fuselage and found that positioning them in locations where the momentum deficit is the largest produced the most reduction on power required. In a comprehensive theoretical and experimental analysis, Hartuc (Ref. 5) found an 18% reduction in shaft power required to drive the propeller when it was positioned in the wake of a fuselage, supporting the claim by Uranga et al. that positioning the propulsive device in a momentum deficit zone can increase performance.

Most of the previous work on BLI propulsion mechanisms has focused on studying the integration for large high-speed transport aircraft (Refs. 6, 7) or has mostly focused on the effect of the integration at a system level for smaller aircraft (Refs. 8–10). Decoupling of the EDF forces for various wing integrations has been given little attention. The rise of novel configurations like the Lilium Jet (Ref. 11) and the Whisper Jet (Ref. 12), enabled by electric propulsion, have opened a field of possibilities for enhanced performance. Novel designs like these will be driven by the underlying physics caused by the aero-propulsive interactions, as these could render some configurations inoperable, due to possible off-axis moments and forces. A study by Kim (Ref. 13) on past blended propulsion-wing concepts concluded that integrating propulsion concepts in the early design stages was integral to obtaining the most benefits and least drawbacks from these integrated EDF architectures.

The purpose of this experimental study was to understand the effects of integrating an EDF on the leading and trailing edge sections of a wing. Both integrations were compared to an EDF in an isolated environment to extract the effects of each integration location on the EDF performance. The two integrations were not directly compared to each other as they have different purposes and applications. The wing integrations considered in this study were not optimized for either position (leading or trailing edge), and merely aim to improve the understanding of the underlying characteristics and the effects on EDF performance (rather than system performance) with each integration, to inform future designs.

Technical Approach

The present study was performed experimentally at Georgia Tech's Low Turbulence Open Jet Wind Tunnel. The test section of the tunnel is 1 m x 1 m, and the tunnel is capable of airspeeds up to 17 m/s. The experiments were performed at a maximum airspeed of 12 m/s due to blockage created by the test article at high angles of attack.

Experimental Setup

Force and moment data of the EDF system were obtained by having the EDF attached in a separate load path connected to a 6-degree of freedom (DOF) load cell. The EDF load cell was mounted directly onto the wing spar, as illustrated in Figures 1(a) and 1(b) for the trailing and leading edge EDF integrations, respectively. This setup provided the unique capability to decouple the forces of the EDF from the ones of the entire system. The EDF was equipped with an electrical power sensor and an RPM sensor to thoroughly characterize its performance.

Figure 1 shows the test rig for the leading-edge integration platform inside the wind tunnel and each integration's mechanical design. Between tests, the EDF integration zone was the only zone changed. The remaining wing sections featured the same airfoil cross-section as the integration platform and extended into the boundary layer of the wind tunnel walls to reduce 3D effects on the propulsor, as shown in Figure 1(c). The test rig was placed at the exhaust of the tunnel to minimize facility effects from the EDF's jet exhaust impinging on the wind tunnel walls, as the EDF's jet exhaust was expected to be between 80 and 100 m/s. This installation permitted the jet to exit with minimal interaction.

The duct geometry, shown in Figure 2, was a revolved Clark-Y airfoil cross section rotated pitch up by 2.3 degrees. This rotation is implemented to maintain a flat profile in the exhaust section. Keeping the exhaust cross-section constant, hence not including any diffusion or contraction. The EDF used for the tests was a Schubeler Technologies DS51-HST EDF. Its characteristics are outlined in Table 1.

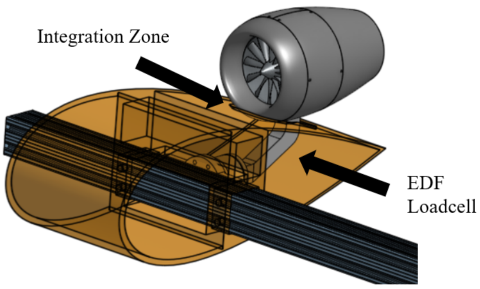

(a) Trailing edge EDF integration for isolated load path

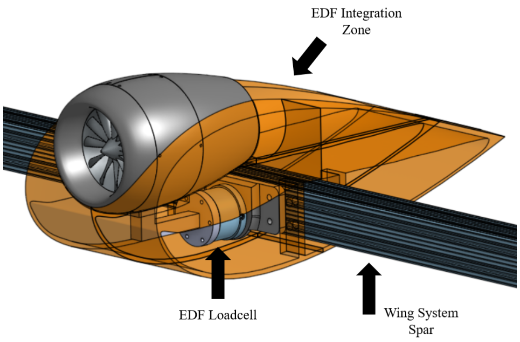

(b) Leading edge EDF integration for isolated load path

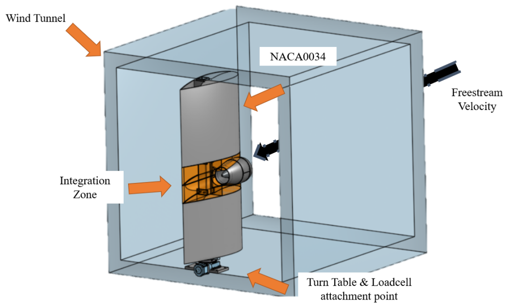

(c) Integration test rig CAD mounted inside tunnel for the leading edge EDF integration case

Fig. 1: EDF integration mechanical design and tunnel integration

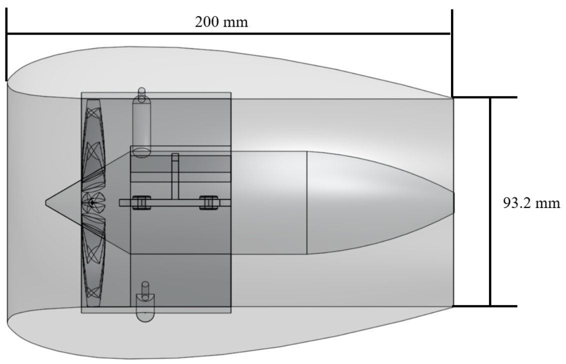

Fig. 2: Tested EDF geometry

Schubeler DS51-HST	
Fan Swept Area	51 cm^2
Weight	640 g
Static Thrust	53 N
Exhaust Speed	93 m/s
Total Efficiency	71%
Number of Blades	12
Rotor Solidity	0.85

Table 1: DS51-HST Characteristics (Ref. 14)

The test rig construction consisted of a 2.5 cm x 2.5 cm steel beam attached to a CNC turntable. The 6-DOF load cell was attached to the mid span of the steel beam through an aluminum bracket to ensure minimal vibrations and bending. The modes of EDF attachment are shown in Figure 3. Through this integration, it was ensured that the loads from the EDF were transferred to the load cell measurement plate. The separation needed to reduce load transfer interference created undesired air gaps, which were reduced by integrating aluminum tape on the edges.

The tight construction and thus the need to run the three-phase power cables in parallel with the load cell cables caused Electromagnetic Interference (EMI). To mitigate this effect, heavy-duty aluminum foil was wrapped around critical components and the power wires were routed outside the wing. Wing loads were outside the scope of this work, hence disturbing the flow away from the EDF was deemed acceptable. Figure 4 shows the EMI reduction system.

Instrumentation and Data Collection

The LabJack T8 was selected as the main load data acquisition device due to its ability to perform simultaneous readings across eight analog channels. The T8 device provides sampling rates up to 48 kHz, making it a suitable tool for unsteady measurements and high-frequency analysis, as is the case in this study. For other sensor data collection such as the DC power and ambient conditions, the LabJack T7-Pro was used, as the lag between measurements was acceptable for these measurements. Additional LabJack T4 were used for the control of the test, with one of the devices controlling the turn table and the other acting as a proportional–integral–derivative (PID) controller for the motor.

To measure the other operational conditions such as the rotational speed, DC voltage, DC current and tunnel temperature, a set of independent sensors were used:

- Interface 6A40A 6-DOF load cell
  - The Interface 6A40A loadcell features maximum loadings of Fx = 200 N, Fy = 200 N, Fz = 500 N, Mx = 5 N-m, My = 5 N-m, and Mz = 5 N-m. Coupled with an in-house built amplifier and the T8, the loadcells measured static loads

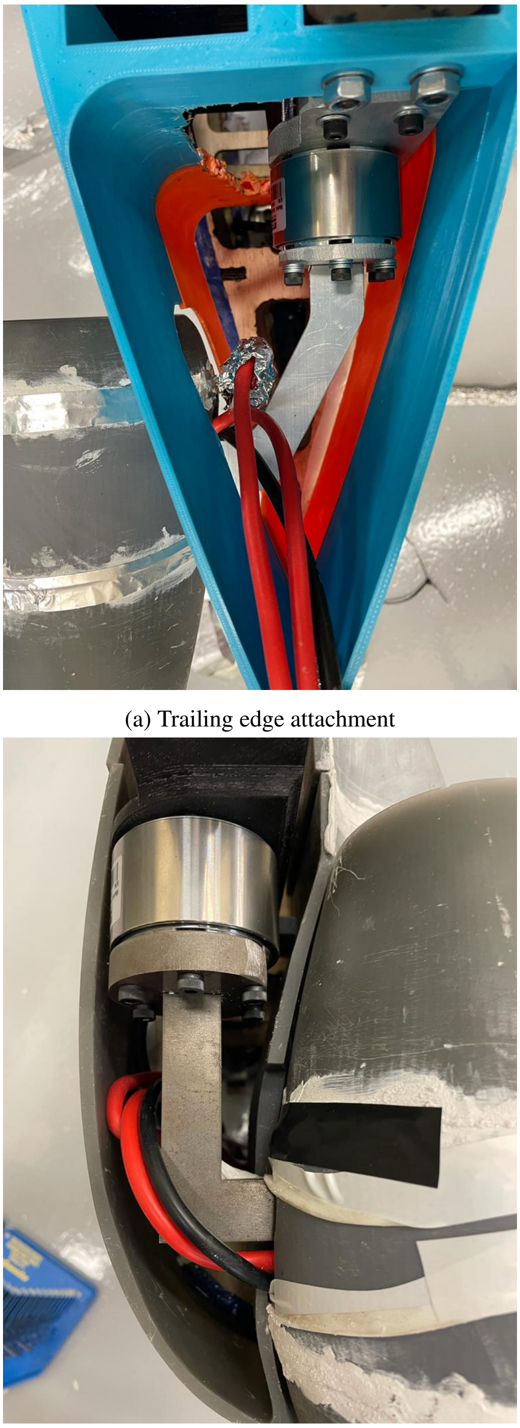

(a) Trailing edge attachment

(b) Leading edge attachment

Fig. 3: EDF load cell connection construction

with a standard deviation of 0.05 N sampled at 10 kHz.

- RPM Sensor
  - The integrated RPM sensor on the Castle Creations HV160-Pro Electronic Speed Controller (ESC) was used.
- DC Voltage
  - To measure DC voltage a simple voltage divider was constructed and placed closely to the ESC to ensure that minimal voltage drop would occur between the sensor and the ESC.
- DC Current
  - To measure DC current, an inline hall effect current sensor manufactured by Allegro Micro Systems (ACS770KCB-400B-PFF-T) was used.
- Temperature
  - The ambient temperature was measured using a 100 K thermistor attached to a voltage divider and powered by the LabJack T7-Pro. The thermistor was set up without any coating to ensure that rapid changes in temperature could be captured. The manufacturer specifies that it is accurate to 0.1 deg.

Test Matrix

The test matrix was designed to explore the EDF behaviour during cruise flight and transition periods (i.e., for eVTOL applications). The angles of attack were limited by geometric constraints of the test facility. Using this test matrix resulted in various advance ratios. The highest advance ratio tested was 0.51. The same test matrix was applied to all studied configurations. The associated advance ratios (J) for each of the studied configurations are shown in Figure 3.

Test Matrix		
Freestream Velocity (m/s)	RPM	Angles of Attack (deg)
5, 7, 10, 12	15k, 20k, 25k	-24 to 24, steps of 2

Table 2: Experimental test matrix for EDF integration test

		RPM		
		15,000	20,000	25,000
Airspeed (m/s)	5	0.215	0.161	0.129
	7	0.301	0.226	0.181
	10	0.431	0.323	0.258
	12	0.516	0.387	0.309

Table 3: Studied advance ratios

The axis definition for the paper is shown in Figure 5. Thrust was defined as the combined forces of the duct and the rotor in the body frame. A matrix transformation was done to translate the measurement origin from the load cell origin to the rotor center of rotation at the rotor plane with the goal to properly study the moment generated by the rotor and the inlet.

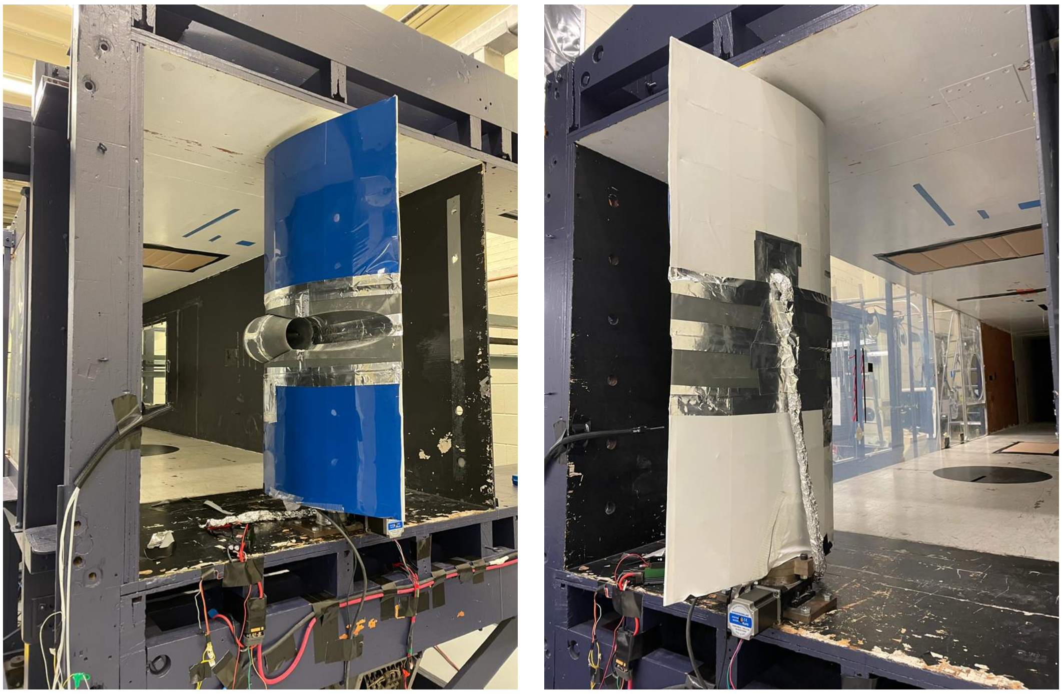

(a) Upper wing surface

(b) Lower wing surface

Fig. 4: Adapted wing construction for EMI mitigation

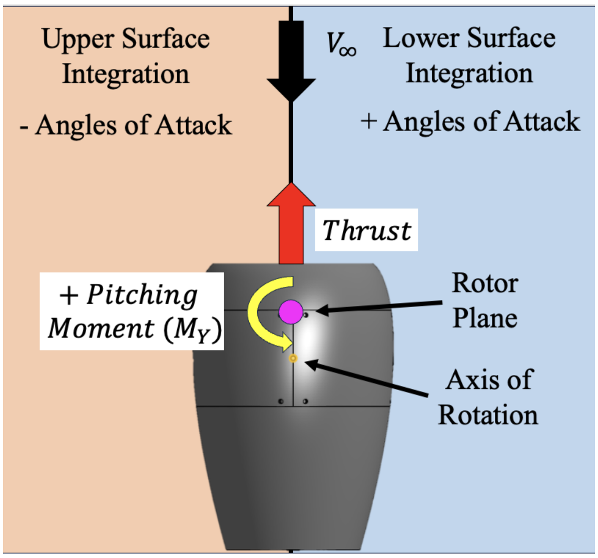

Fig. 5: Axis definition

Results and Discussion

This section is divided by measurement type. The most important measurements that are discussed are the thrust coefficient measurement and pitching moment at the rotor plane. The power loading is analyzed as the overarching performance metric. Lastly, the results of high-frequency measurements and acoustic measurements are discussed through a short-time Fourier transform (STFT).

All measurements discussed in this section have been transformed to be relative to the rotor plane and axis of rotation. For brevity, the entirety of the results are not shown for repeatable trends. The plots shown in the section are representative of the test matrix and were chosen to showcase repeatable trends observed during the testing campaign. Error bars shown represent one standard deviation of the average of the independent tests.

Thrust Coefficient

The thrust coefficient is preferred to the dimensional thrust for analysis to account for various environmental conditions observed for different testing days. The rotorcraft convention was selected for non-dimensionalization. Note that the thrust force includes both the rotor and duct forces.

Leading Edge Integration Figure 6 shows the thrust coefficient with respect to the angle of attack for various RPM cases for the leading edge integration. The isolated duct thrust coefficients are shown with lines, while the integrated thrust coefficients are shown with markers. The integrated EDF exhibits a similar behavior as the isolated EDF for all cases at 5 m/s, as shown in Figure 6(a). When the freestream velocity is increased to 10 m/s, the integrated EDF behavior deviates from the isolated EDF (Figure 6(b)). At higher advance ratios (lower RPM for same airspeed), the minimum thrust coefficient angle of attack shifts towards the positive angles of attack (a pitch down angle for this reference). For both the upper and lower integration cases, the isolated EDF produces more thrust than the integrated version, except for the 15k RPM at 10 m/s, for which the minimum thrust has similar magnitude.

Trailing Edge Integration Figure 7 shows the thrust coefficient vs. angle of attack for various RPM cases for the trailing edge integration and the isolated EDF. As observed for the leading edge integration cases, the integrated EDF produces less thrust coefficient than the isolated EDF. This can be attributed to the increased local flow speed generated by the wing. This effect is shown in Figure 7(b), where the upper surface integration (negative angles of attack) produces less thrust coefficient due to higher local airspeeds. The effect is most notable for the high RPM case because the higher inflow velocities generated by the higher RPM delays separation over the wing and further increases its local velocity. Note the increased unsteadiness of the measurements for the upper integration at higher freestream velocities. This is attributed to the increased unsteadiness of the wing's boundary layer as it approaches a separation state. For the lower airspeed cases, the rotor inflow velocity dominates the flow field and controls separation in the measured cases.

Pitching Moment, M_Y

The pitching moment is presented in its dimensional form. For the EDF loads, pitching moment is a combination of the rotor pitching moment due to asymmetric inflow and the imbalance of the inlet thrust forces. The rotorcraft non-dimensionalization did not show useful trends to characterize the behaviour.

The isolated EDF data (Figure 8) shows the dominance of the inlet forces on the generation of pitching moment. For rotors, the moment observed at the rotor plane is expected to be a restoring moment towards the 0 angle of attack condition. The flow accelerates over the inlet lip (if not separated) causing higher inflow velocities in the windward side of the duct. This effect causes lower thrust on the windward side of the rotor disk, hence generating a stabilizing moment due to thrust imbalance. The inlet on the other hand, produces a destabilizing moment. The windward side of the inlet produces more streamwise force than the leeward. In addition, the leeward side of the duct acts more as an airfoil, hence producing a large tangential force that aids the destabilizing behavior. Figure 8 shows dominance of the destabilizing moment over the rotor generated stabilizing moment. The behavior can be seen at the higher angles where the pitching moment is positive.

Leading Edge Integration Figure 8 shows that the leading edge integration exhibited similar behavior as the isolated EDF for the upper integration. That behavior is expected as the duct is in a similar configuration as the isolated. In the case of the lower integration, the behavior is mostly constant. The leeward side of the duct is integrated into the wing, reducing the produced tangential force to zero, and the inlet destabilizing moment reduces to only the

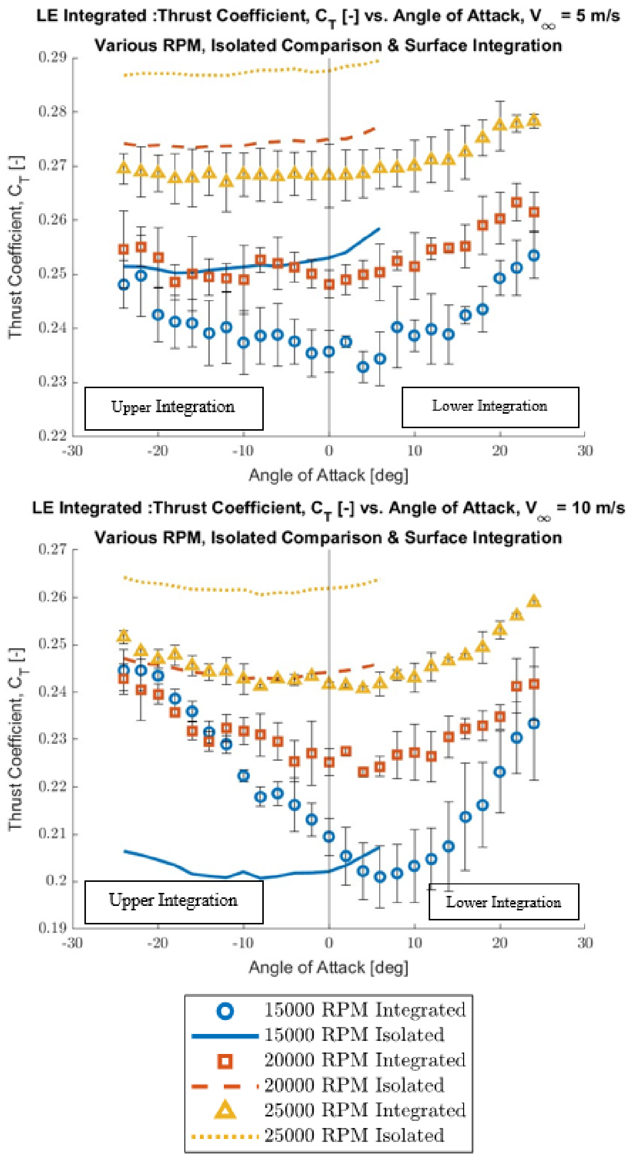

Fig. 6: Thrust coefficient for leading edge integration at various conditions compared to isolated EDF for both surface integrations. Top figure at 5 m/s and bottom at 10 m/s

streamwise force imbalance. This behavior is replicated for all airspeeds and RPM. The destabilizing and stabilizing moments must increase at similar rates to create the angle independent destabilizing moment.

Trailing Edge Integration Figure 9 shows the pitching moment with respect to angle of attack for the trailing edge integrated EDF. The results show a pitching down moment across all the studied angles. From a rotor forces perspective, the side of the duct ingesting the boundary layer (BL) would cause higher thrust, hence a positive moment. The experimental results shown in Figure 9 give insight on the dominance of the duct forces for these testing conditions: the side of inlet attached to the wing's surface is not producing any streamwise force while the one on the freestream does, generating a dominating force imbalance

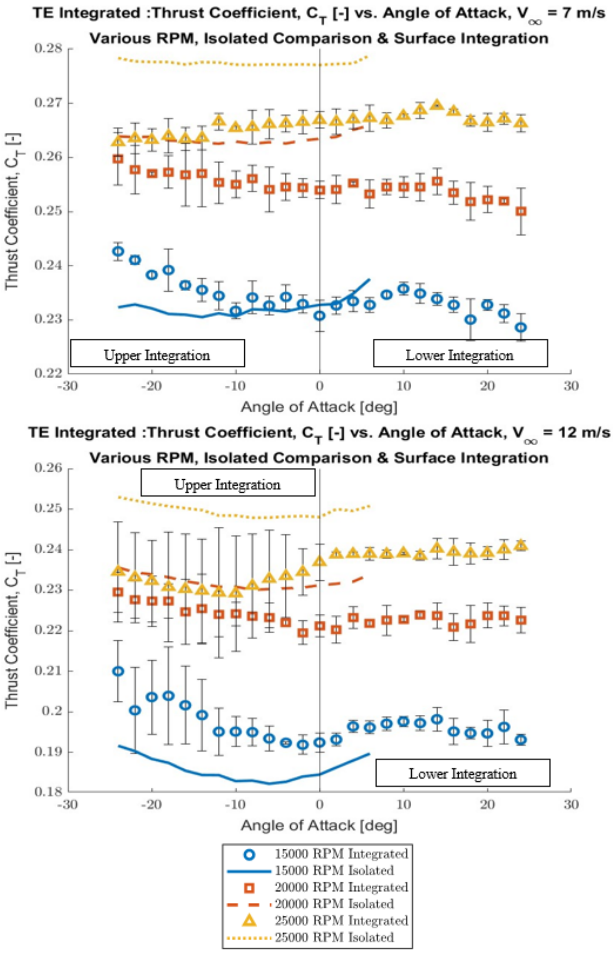

Fig. 7: Thrust coefficient for trailing edge integration at various conditions compared to isolated EDF for both surface integrations. Top figure at 7 m/s and bottom at 10 m/s

that leads to the observed behaviour.

Performance Analysis

The performance metric used in this study was the non-dimensional power loading (C_T/C_P).

Leading Edge Integration Figure 10 shows the performance comparison for the leading edge integration configuration. For the lower airspeeds, while the trends between the isolated and integrated EDF match, the isolated EDF has better performance at the lower advance ratios. For the higher airspeeds, the trend flips with the integrated EDF having better performance. Based on the data, the increase in performance difference is dependent on the EDF advance ratio. This trend could be attributed to the coverage of the duct surface due to its integration by reducing the parasite drag at higher airspeeds.

Trailing Edge Integration Figure 11 shows the performance of the EDF in the trailing edge configuration. Similar to the leading edge integration, the benefit in performance of the integration is mostly seen at higher advance

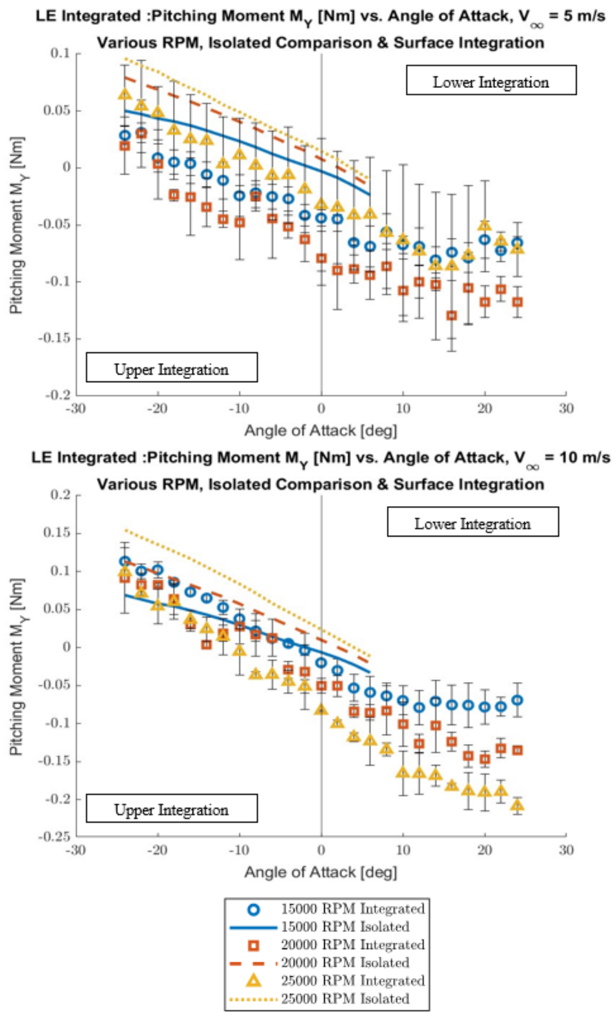

Fig. 8: Pitching moment for leading edge integration at various conditions compared to isolated EDF for both surface integrations. Top figure at 5 m/s and bottom at 10 m/s

ratios.

DC Power Required

The power required is presented as a dimensional magnitude, although the percentage differences between dimensional and non-dimensional remain the same.

Leading Edge Integration Figure 12 shows the power required at 12 m/s at various RPM for the leading edge integration. The overall power required was less for the integrated version than for the isolated EDF. This could be attributed to the acceleration of the flow caused by the presence of the wing. Similar to what was observed in the performance trends, the percentage difference between the isolated and the integrated version was a function of the advance ratio. More power required benefit was observed for the lower RPM (higher advance ratio). For the 12 m/s case, the average power required benefit for the 25k RPM case was 5%, 20k RPM 5%, and 15k RPM was 8%.

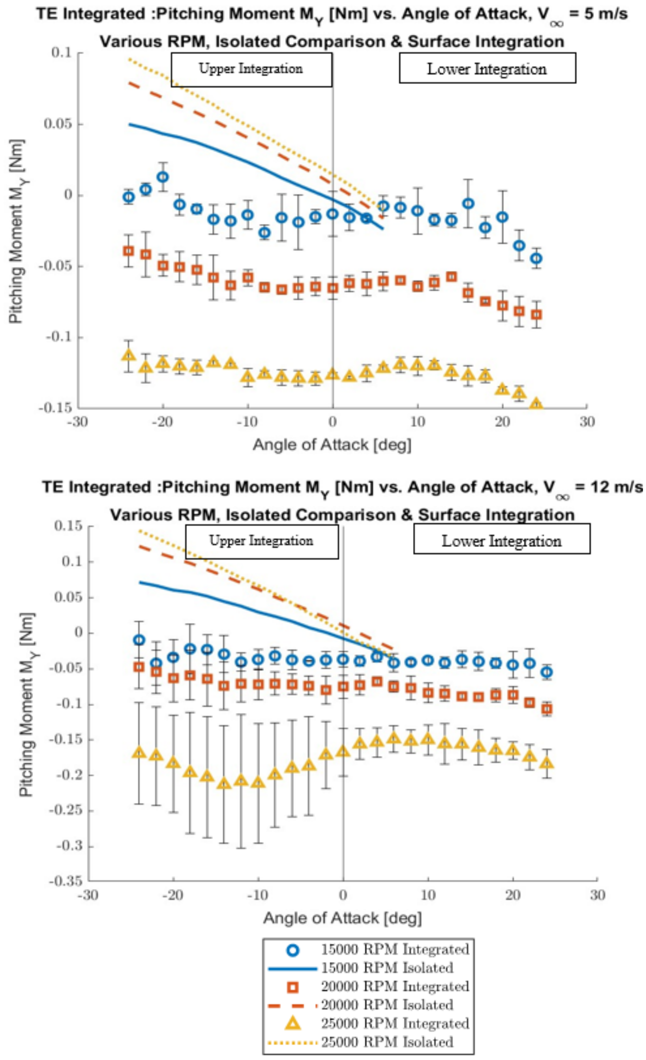

Fig. 9: Pitching moment for trailing edge integration at various conditions compared to isolated EDF for both surface integrations. Top figure at 5 m/s and bottom at 12 m/s

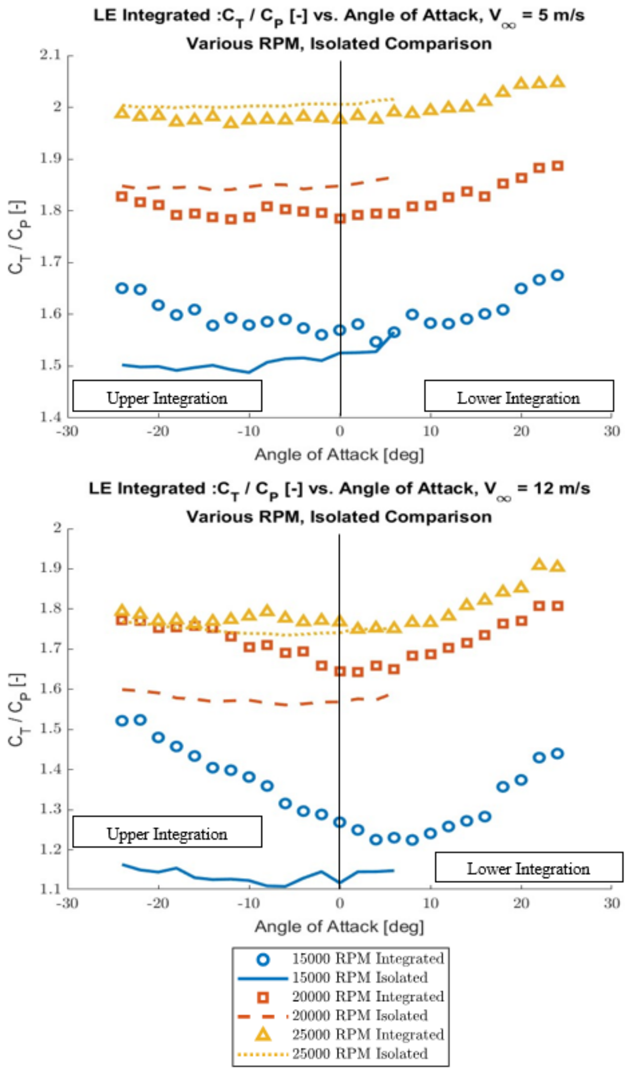

Fig. 10: Non-dimensional power loading for leading edge integration at various conditions compared to isolated EDF for both surface integrations. Top figure at 5 m/s and bottom at 12 m/s

Trailing Edge Integration Figure 13 shows the power required at 12 m/s at various RPM for the trailing edge case. The trends are similar to the ones for the leading edge case, and are therefore not described for brevity. In this case, the average power required benefit for the integration was 7% for the 25k RPM, 9% for 20k RPM, and 12% for 15k RPM.

High-Frequency Loads and Acoustics

The high-frequency section of this results section analyzes the different integration configurations in the same figures as it is beneficial to understand common frequencies. With all configurations in the same figures, observed different resulting frequencies must be unique to the studied configuration.

Figure 14 shows the high frequency measurements for 12 m/s at 25k RPM case at various angles of attack. Figure 15 shows the acoustic high frequency measurements for the same testing conditions as the loads. Note that the two measurements were taken during the same experiment runs but are not time synced.

Leading Edge Integration The middle column of Figure 14 shows the data at 0 angle of attack. The dominant frequencies observed from the leading edge integration case and the isolated EDF match. The dominant frequencies present on those cases are 14 kHz, 9 kHz, 4 kHz, and 2.5 kHz. The RPM frequency is also present but it is not observable at this scale. When comparing to the acoustic high-frequency data shown in Figure 15, the 14kHz frequency appears at a lesser magnitude but its repeatability shows that the frequency must be associated to an aerodynamic effect. The acoustic data also shows a dominant frequency of 5 kHz across all configurations, a frequency that is not dominant in the loads. This could be attributed to an internal bearing sound, which would have a noticeable

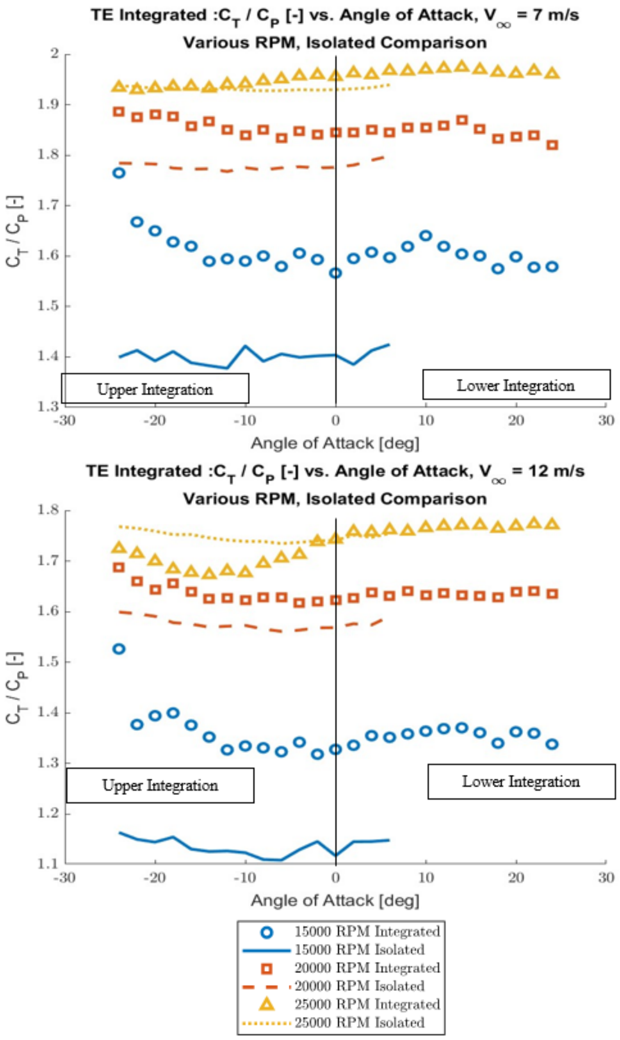

Fig. 11: Non-dimensional power loading for trailing edge integration at various conditions compared to isolated EDF for both surface integrations. Top figure at 7 m/s and bottom at 12 m/s

acoustic effect but a minimal effect on the loads.

Trailing Edge Integration The bottom row of both Figures 14 and 15 show the high frequency data collected for the trailing edge integration. In Figure 14, this integration exhibits new dominant frequencies at 12.3 kHz, 11.8 kHz, and 10.7 kHz, which persist regardless of the angle of attack of the wing. These frequencies could be the frequencies at which the unsteadiness of the boundary layer is being ingested. For these testing conditions, complete stall was never achieved, which could explain why the frequencies are constant for the various angles of attack. As noted before, the acoustic data shows a dominant frequency at 5 kHz present for all the cases. Most of the dominant frequencies are below 5kHz for the trailing edge, with dominant frequencies showing at 2.4 kHz and 4.8 kHz. These also appear on the loads high frequency analysis, pointing to an aerodynamic phenomena.

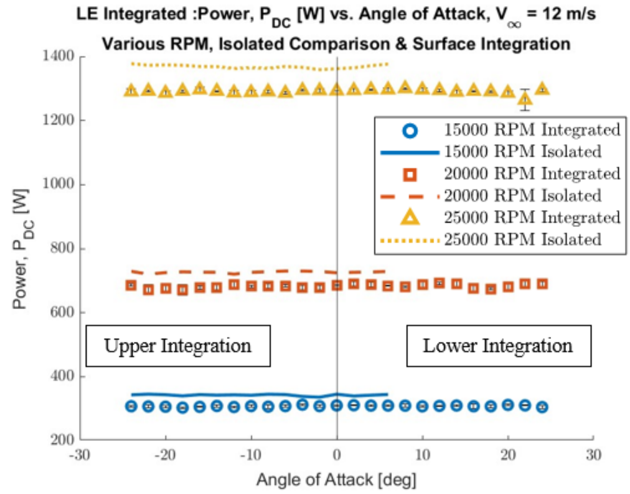

Fig. 12: DC power required for leading edge integration at various conditions compared to isolated EDF for both surface integrations at 12 m/s

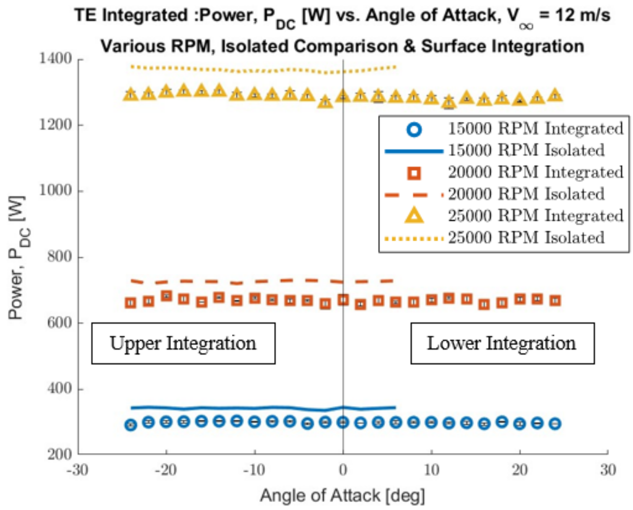

Fig. 13: DC power required for trailing edge integration at various conditions compared to isolated EDF for both surface integrations at 12 m/s

Conclusions

This study focused on understanding the changes in performance that various integrations of an electric ducted fan (EDF) on a wing caused. The comparison was done between leading and trailing edge integrated EDFs and the isolated baseline version. A direct comparison between leading and trailing edge integrations was not in the scope of this paper, as the integration was neither optimized for leading nor trailing edge integration. To compare efficiency, the non-dimensional power loading was used. A high-frequency analysis was performed to explore the dominant frequencies for each integration. The frequency analysis was done on both loads and acoustic data and a short-time Fourier transform was used to analyze the data.

The leading edge integrated EDF produced a lower thrust coefficient than the isolated EDF in most testing con-

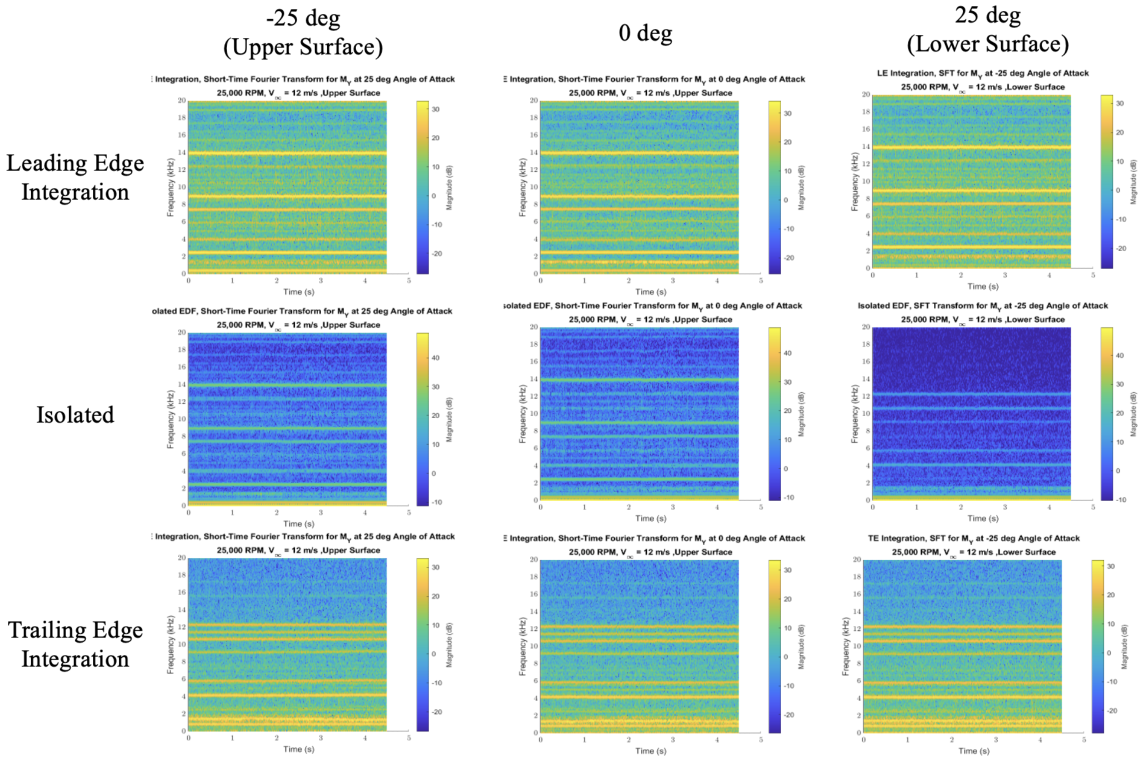

Fig. 14: High frequency loads analysis (M_Y) at various conditions compared to isolated EDF for both surface integrations at 12 m/s

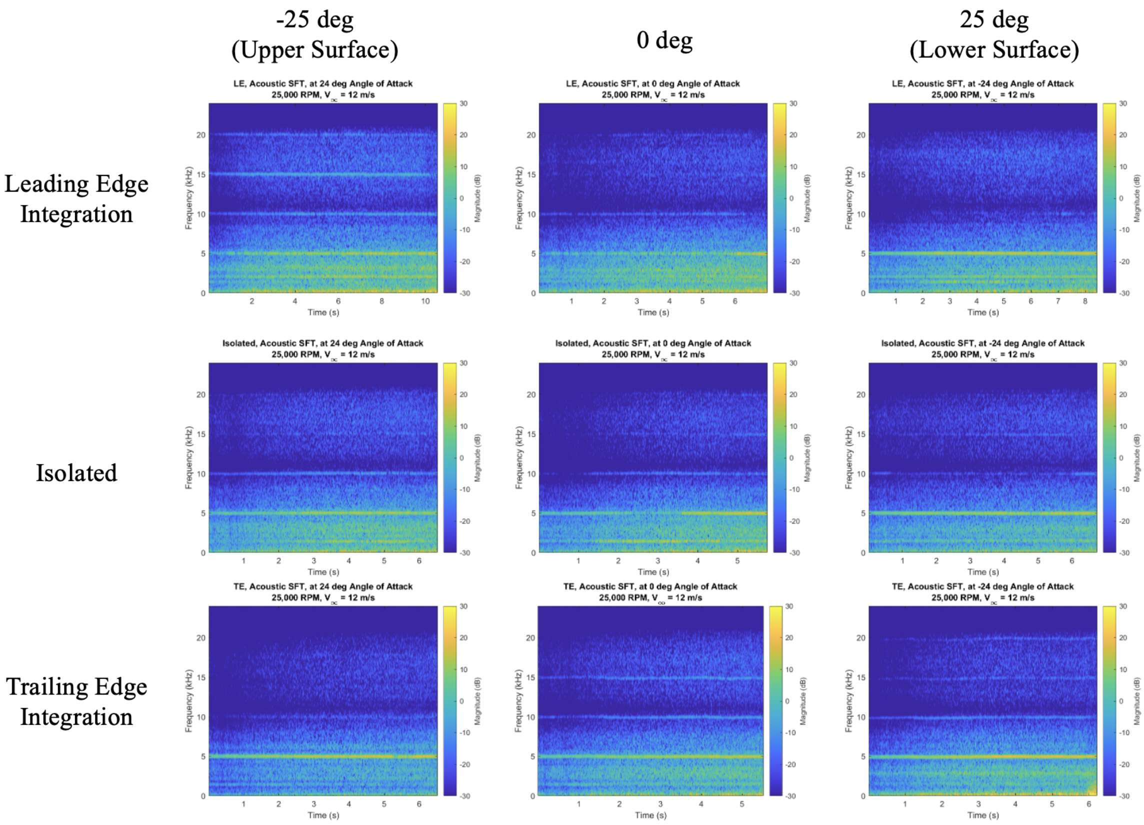

Fig. 15: High frequency acoustics at various conditions compared to isolated EDF for both surface integrations at 12 m/s

ditions. The difference in thrust coefficient grew with increasing advance ratio. At higher advance ratios, the angle at which the minimum thrust coefficient occurs moved towards a pitch-down angle. The maximum value observed was a change of eight degrees pitch down at the highest advance ratio that was studied. This means that for higher advance ratios, the thrust coefficient of the EDF increased for the cruise condition (0 degrees angle of attack).

Overall, the power loading of the leading edge integrated EDF increased in comparison with the isolated EDF for the higher advance ratios. The maximum increase in power loading observed was 10.91% for the cruise condition at 15k RPM at 12 m/s. In the cases of the lower advance ratios studied, the overall efficiency decreased with relation to the isolated case. The largest decrease observed was 2.78% for the 20k RPM case at 5 m/s.

The pitching moment behavior was similar to the isolated EDF for the upper surface integration, but the lower surface integration showed a constant destabilizing behaviour that was independent from angle of attack. This behaviour was attributed to the leeward inlet lip being covered due to the integration. The high-frequency analysis for the leading edge integration showed similar dominant frequencies as for the isolated EDF for both the loads and acoustics data.

Similar to the leading edge integration, the thrust coefficient increased with advance ratio but in most of the studied cases the isolated thruster had a higher thrust coefficient. For the thrust, the higher the advance ratio, the more similar it was to the isolated case. The largest thrust coefficient increase was observed at the highest advance ratio studied (15k RPM at 12 m/s) with an increase of 4.46% in the cruise condition. The largest drop in thrust coefficient was observed at the lowest advance ratio studied in the condition of 25k RPM at 5 m/s with a drop of 3.88%.

In terms of power loading, C_T/C_P, the trailing edge integrated EDF performed better than the isolated EDF in all cases. The change in performance was also a function of advance ratio: the higher the advance ratio, the larger the increase in performance. The largest increase observed was 22.05% for the upper surface integration at 18 degrees at 15k RPM in a 12 m/s freestream.

The pitching moment of the trailing edge integrated EDF was mostly constant at a negative value with a reduced dependence on angle of attack. This result shows the dominance of inlet lip forces even with a thrust asymmetry on the rotor (due to reduced velocities from the wing boundary layer). The high-frequency analysis showed the existence of new high frequencies (15 kHz range) and low frequencies (1 kHz - 2 kHz) in comparison to the isolated EDF. These frequencies are most likely from the unsteadiness associated with ingesting the wing boundary layer. The unsteadiness in the flow causes thrust asymmetry, oscillatory loads and inlet force unsteadiness.

Overall, both integration methods showed increases in performance and power reduction over the isolated EDF. Each configuration presents its own characteristics that could influence the preferred system integration. Understanding the underlying physics of the integrated EDF system for distinct operational conditions may inform future design methods for emerging regional air mobility platforms.

Acknowledgements

The authors would like to thank Mihir Sahah for his assistance in performing the experimental tests and component manufacturing. The authors would also like to thank Carlota Bonnet for her assistance on this project.

Contact Information

The authors are affiliated with Daniel Guggenheim School of Aerospace Engineering, Georgia Institute of Technology.

dsafieh@gatech.edu

juergen.rauleder@gatech.edu

REFERENCES

[1] Lawrence, I., "London is only the SIXTH worst city in the world for commuters," 2022, https://www.timeout.com/london/news/london-is-only-the-sixth-worst-city-in-the-world-for-commuters-100722.

[2] EEA, "CO2 Emissions from Passenger Transport," https://www.eea.europa.eu/media/infographics/co2-emissions-from-passenger-transport/view, 2020, Accessed: 2023-02-15.

[3] IATA, "Net Zero 2050: New Aircraft Technology," https://www.iata.org/en/iata-repository/pressroom/fact-sheets/fact-sheet-new-aircraft-technology/, 2021, Accessed: 2023-02-15.

[4] Uranga, A., Drela, M., Greitzer, E., Titchener, N., Lieu, M., Siu, N., Huang, A., Gatlin, G. M., and Hannon, J., "Preliminary Experimental Assessment of the Boundary Layer Ingestion Benefit for the D8 Aircraft," *AIAA Scitech 2014 Forum*, National Harbor, MD, 2014.

[5] Hartuc, T., *Boundary Layer Ingestion: Theoretical and Experimental Research*, Ph.D. thesis, TU Delft, Delft, The Netherlands, 2015, https://repository.tudelft.nl/islandora/search/author%3A%22Hartu%C3%A7%2C%20T.%22?collection=education.

[6] Seitz, A., Habermann, A., Peter, F., Troeltsch, F., Castillo Pardo, A., Della Corte, B., van Sluis, M., Goraj, Z., Kowalski, M., Zhao, X., Grönstedt, T., Bijewitz, J., and

Wortmann, G., “Proof of concept study for fuselage boundary layer ingesting propulsion,” *Open Access Aeronautics and Astronautics Journal, 8 (1), 1-65*, Vol. 8, No. 1, 2021, pp. 1–65.

[7] Uranga, A. and Drela, M., “Preliminary Experimental Assessment of the Boundary Layer Ingestion Benefit for the D8 Aircraft,” *52nd Aerospace Sciences Meeting*, National Harbor, MD, January 2014.

[8] Perry, A., Bretl, T., and Ansell, P., “System Identification of a Subscale Distributed Electric Propulsion Aircraft,” *Journal of Aircraft*, Vol. 60, No. 3, 2023.

[9] Perry, A., Bretl, T., and Ansell, P., “Aeropropulsive Coupling Effects on a General-Aviation Aircraft with Distributed Electric Propulsion,” *Journal of Aircraft*, Vol. 58, No. 6, 2021, pp. 1–14.

[10] Perry, A., Ansell, P., and Kerho, M., “Aero-Propulsive and Propulsor Cross-Coupling Effects on a Distributed Propulsion System,” *Journal of Aircraft*, Vol. 55, No. 6, 2018, pp. 1–13.

[11] Lilium, “Lilium Jet,” `https://lilium.com/jet`, 2023, Accessed: 2023-07-16.

[12] Loz Blain, “Whisper Aero claims radical advance in quiet, efficient electric jets,” `https://newatlas.com/aircraft/whisper-aero-quiet-electric-propulsion/`, 2023, Accessed: 2023-07-16.

[13] Kim, H. D., “Distributed Propulsion Vehicles,” *27th International Congress of the Aeronautical Sciences*, Nice, France, 19-24 September 2010.

[14] Schuebeler Technologies, “DS51-HST,” `https://www.schuebeler-tech.com/product/ds-51-dia-hst/?v=7516fd43adaa`, 2022, Accessed: 2023-02-16.